11-15-2022

Spatial origin analysis on atmospheric bulk deposition of polycyclic aromatic hydrocarbons in Shanghai

Ying Liu

Xiaomin Zhang

Jianguo Tan

Peter Grathwohl

Rainer Lohmann
University of Rhode Island, rlohmann@uri.edu

Citation/Publisher Attribution

Liu, Ying, Xiaomin Zhang, Jianguo Tan, Peter Grathwohl, and Rainer Lohmann. Spatial origin analysis on atmospheric bulk deposition of polycyclic aromatic hydrocarbons in Shanghai. *Env Poll*, 313 (2022) 120162. https://doi.org/10.1016/j.envpol.2022.120162

Spatial origin analysis on atmospheric bulk deposition of polycyclic aromatic hydrocarbons in Shanghai

YING LIU [†,‡,#,*], XIAOMIN ZHANG [†,#], JIANGUO TAN [‡,Δ], PETER GRATHWOHL [§], RAINER LOHMANN [Φ]

[†] *State Key Laboratory of Pollution Control and Resource Reuse, College of Environmental Science and Engineering, Tongji University, Shanghai 200092, China*

[‡] *Key Laboratory of Cities' Mitigation and Adaptation to Climate Change, Shanghai, China Meteorological Administration (CMA), Tongji University, Shanghai 200092, China*

[#] *Key Laboratory of Yangtze River Water Environment, Ministry of Education, College of Environmental Science and Engineering, Tongji University, Shanghai 200092, China*

[Δ] *Shanghai Meteorological IT Support Center, Shanghai Meteorological Service, Shanghai 200030, China*

[§] *Department of Geosciences, University of Tübingen, Schnarrenbergstraße 94-96, 72076 Tübingen, Germany*

[Φ] *Graduate School of Oceanography, University of Rhode Island, Narragansett, Rhode Island 02882-1197, United States.*

* To whom correspondence should be addressed

E-mail address: liu_ying@tongji.edu.cn (YL)

ABSTRACT

Atmospheric deposition of polycyclic aromatic hydrocarbons (PAHs) onto soil threatens terrestrial ecosystem. To locate potential source areas geographically, a total of 139 atmospheric bulk deposition samples were collected during 2012 – 2019 at eight sites in Shanghai and its surrounding areas. A multisite joint location method was developed for the first time to locate potential source areas of atmospheric PAHs based on an enhanced three dimensional concentration weighted trajectory model. The method considered spatial and temporal variations of atmospheric boundary layer height and homogenized all results over the eight sites via geometric mean. Regional transport was an important contributor of PAH atmospheric deposition while massive local emissions may disturb the identification of potential source areas. Northwesterly winds were associated with elevated deposition fluxes. Potential source areas were identified by the multisite joint location method and included Hebei, Tianjin, Shandong and Jiangsu to the north, and Anhui to the west of Shanghai. PM and SO_2 data from the national ground monitoring stations confirmed the identified source areas of deposited PAHs in Shanghai.

KEYWORDS

trajectory sector analysis; spatial origin analysis; planetary boundary layer height;

1 INTRODUCTION

The ubiquitous occurrence of polycyclic aromatic hydrocarbons (PAHs) in the atmosphere is due to their massive emissions from pyrogenic and petrogenic sources, such as fuel combustion and petroleum evaporation (Dumanoglu et al., 2017; Lammel, 2015; Liu et al., 2015), and long-range transport in the atmosphere (Hu et al., 2021; Keyte et al., 2013). Atmospheric deposition results in accumulation of PAHs in surface soils, which threatens terrestrial ecosystems (Degrendele et al., 2016; Jia et al., 2019). In order to reduce the risk from PAH deposition, it is necessary to locate the geographic source areas of atmospheric PAHs and then propose effective abatement strategies. Many studies have used Lagrangian trajectory models (e.g., HYSPLIT) to track pathways of air parcels (Hosseini Dehshiri et al., 2022; Stein et al., 2015; Sun et al., 2017) and locate source areas of atmospheric pollutants (e.g., $PM_{2.5}$ and SO_2) via probabilistic models, e.g., concentration weighted trajectory (CWT) and potential source contribution function (PSCF) models (Polissar et al., 2001; Sheng et al., 2013; Zhang et al., 2019). But only a few studies conducted the spatial location of emission source areas for atmospheric deposition of PAHs, for example, by discussing the influence of monsoon or correlations with air-mass backward trajectories (Arellano et al., 2018; Hu et al., 2021), possibly due to the lack of high frequency data or a limited sample size (i.e., < 100 samples per site) to support the probabilistic models (Hafner and Hites, 2003). Spatial origin analysis for atmospheric pollutants with a high frequency of measurement (e.g., $PM_{2.5}$) is possible if near surface local emissions are absent, e.g., at high mountains (Huang et al., 2021), rural areas (Dimitriou et al., 2021), or remote background sites (Liu et al., 2019; Suzuki et al., 2021); otherwise, concentration time series reflect time variation of local emissions rather than regional transport. Normally, a background site should be located upwind of local emissions, but seasonal changes in wind direction may interfere with the idea of fixed location background sites (Pu et al., 2020). In addition, low frequency measurements for deposition fluxes of PAHs in a probabilistic model could lead to large uncertainties in spatial origin analysis due to the limited sample size. This prompted us to develop a multisite joint location approach based on the CWT model to identify potential source areas of atmospheric deposition of PAHs in

Shanghai.

Most prior studies implemented the CWT or PSCF model on gridded two dimensional maps (Bao et al., 2019; Wang et al., 2009; Zhao et al., 2020). Few reports involved altitudinal characteristics of air masses in backward trajectories, for example, based on arbitrary threshold heights of the atmospheric boundary layer (Dimitriou et al., 2021; 2022; Kim et al., 2016) or concentration weighted boundary layers (Stojic and Stojic, 2017). The planetary boundary layer (PBL) is the layer above the earth surface where vertical transports by turbulence play a dominant role in the transfers of heats, moistures, and air pollutants; the planetary boundary layer height (PBLH) varies with time, location, and weather conditions (Charlson, 2000). Air pollutants released from ground sources are restricted within the boundary layer and the PBLH can weaken the exchange of air pollutants between the boundary layer and free troposphere (Qu et al., 2017). The influence of planetary boundary layer cannot be ignored in atmospheric transport analysis (Li et al., 2021b; Miao et al., 2021), not only at receptor sites, but also at each segment along back trajectories. Hence, the spatial and temporal variation of planetary boundary layer height needs to be fully considered in the spatial origin analysis.

Atmospheric deposition of PAHs has been extensively studied in Shanghai (Cheng et al., 2018; Lian et al., 2009; Liang et al., 2016; Wang et al., 2016; Yan et al., 2012). Our previous work revealed that deposition fluxes of PAHs in Shanghai during 2012 – 2014 was categorized as moderate to high on a global scale; its variation was attributed to meteorological conditions and local emissions from urban space and industries (Feng et al., 2017). This observation was extended through 2019 (stopped due to the COVID-19 pandemic) and a total of 139 samples were collected, which provided us an opportunity to develop a new method for spatial origin analysis via combining the 139 samples collected from eight monitoring sites. The goals of this study therefore were to (a) analyze time series of PAH deposition fluxes from 2012 to 2019 in Shanghai, (b) assess contribution of regional transport, (c) screen spatial directions of regional transport, and (d) develop a multisite joint location method to identify potential source areas of atmospheric PAHs deposited into Shanghai.

2 MATERIALS AND METHODOLOGY

2.1 Sampling

Eight atmospheric bulk deposition samplers of PAHs were deployed during 2012 – 2019 in Shanghai city (SH1 – SH6), Jiaxing city (JX) of Zhejiang province, and Haimen city (HM) of Jiangsu province, as shown in Figure 1. Due to logistical constraints (or possible vandalism), some of samplers were destroyed, lost or had to be added. A total of 139 atmospheric deposition samples were collected in 9 – 22 campaigns lasting for 30 – 149 days each. More detailed information on sampling campaigns is listed in Table S1 of the Supporting Information (SI). The atmospheric bulk deposition sampler has been described previously (Feng et al., 2017) and was comprised of a borosilicate glass funnel (12.3 L volume with a 0.049 m^2 of cross-sectional area) and an adsorption cartridge, packed with 15 g of Amberlite IRA – 743 with glass wool plugs at the top and the bottom (25 mm I.D. and 210 mm length). PAHs in atmospheric dry and wet depositions were collected by filtration of glass wools and adsorption of IRA – 743 adsorbents. The sampler was fixed in a metal box at the height of 1.5 – 2.0 m above the ground. The sampler has been designed to effectively collect and filter rainwaters, even in heavy rain events.

2.2 Sample analysis and quality control

As for the sampling campaigns before 2016, sample processing followed an established method (Feng et al., 2017), i.e., acetone rinsing for removing rainwater in samples followed by Soxhlet-extraction (PAHs dissolved in the acetone extract were liquid-liquid extracted). Samples collected after 2016 were treated by a slightly modified method, including field surrogate labeling (deuterated pyrene was spiked into adsorbents to evaluate potential breakthrough in field sampling), freeze drying for water removal coupled with Soxhlet-extraction. Five deuterated PAHs were spiked to extracts as lab surrogates before the liquid-liquid and Soxhlet extractions. After silica cleanup, samples underwent GCMS analysis and lab surrogate correction. More details are presented in the SI.

Average recoveries of lab surrogate standards (five deuterated PAHs) were 22 – 94% and 42 – 95% in the liquid-liquid extraction and Soxhlet extraction,

respectively, for the samples collected before 2016; while in the modified method lab surrogates' recoveries increased to 44 – 97% and field surrogate's recoveries (deuterated pyrene) were 83 ± 17%. At least one of field blanks was employed for quality assurance in each sampling campaign. Except for naphthalene (up to ca 80%), target PAHs in the blanks accounted for < 10% of average concentrations detected in atmospheric deposition samples (see Table S2). Limits of detection of PAH deposition fluxes were 0.23 – 12.5 ng m^{-2} day^{-1} (see Table S2) based on three times standard deviation of PAH concentration in field blanks (0.049 m^2 of cross-sectional area and 60 days of common duration time). More details on quality assurance and quality control are given in the SI.

2.3 Time series analysis

Following the statistical approach of Hites (2021), a time series of atmospheric deposition fluxes of PAHs ($\boldsymbol{F_t}$ in ng m^{-2} day^{-1}) was analyzed via a first-order rate equation (Eq. 1); half-life time ($\boldsymbol{T_{0.5}}$ in years) and 95% confidence interval were used to describe time trend and its uncertainty (see Eq. 2).

$$ln(F_t) = a_0 + a_1 \times t \quad (1)$$

95% confidence interval:

$$T_{0.5} \pm 2 \times SD_{T_{0.5}} = -\frac{ln(2)}{a_1} \pm 2 \times (-\frac{ln(2)}{a_1}) \times \left(\frac{SD_{a_1}}{a_1}\right) \quad (2)$$

where $\boldsymbol{a_0}$ *and* $\boldsymbol{a_1}$ (in $year^{-1}$) indicates respectively fitting parameters, $\boldsymbol{t}$ is the sampling date (time, in years), and $\boldsymbol{SD}$ denotes the standard deviation.

2.4 Backward trajectories of air masses and planetary boundary layer heights

72-hour backward trajectories of air masses during sampling campaigns for each site were calculated by the Hybrid Single Particle Lagrangian Integrated Trajectory model (HYSPLIT) developed by the NOAA's Air Resources Laboratory; Global Data Assimilation System (GDAS) archive data were provided by the US National Weather Service's National Centers for Environmental Prediction. For each day, one backward trajectory ending at a height of 500 m above ground level (AGL) of sampling site was produced at the 14:00 local time (UTC + 8h) due to

the hourly maximum values of PBLH occurred at this time (Li et al., 2021a; Peng et al., 2017).

Additionally, global planetary boundary layer heights (PBLH) were reanalyzed from July to December of 2018 by the ECMWF ERA – Interim model (Dee et al., 2011) and described statistically in Figure S5 via a Cell Statistics tool of ArcGIS at a time resolution of 3 h and a spatial resolution of 0.5° × 0.5°, considering altitudinal characteristics of air masses to produce a geographical overview of emission source areas.

2.5 Enhanced three dimensional concentration weighted trajectories (3D – CWT)

The total number of trajectory endpoints from the HYSPLIT model ranged from 48,837 (73 endpoints per trajectory × 1 trajectory per day × 669 days) at SH5 to 140,014 (73 × 1,918) at SH4 and these endpoints were located in a geographical domain of 38,192 (i.e., 248 columns × 154 rows) grid cells with a 0.5° × 0.5° resolution between 32 °E – 156 °E in longitude and 3 °N – 80 °N in latitude. Based on traditional 2D – CWT model (Masiol et al., 2019; Wei et al., 2019), a key modification in this study is embodied in an altitudinal dimension of air masses, which weights the influence of planetary boundary layer on atmospheric transport of PAHs. Briefly, the geographical domain is further divided into five vertical layers allowing to differentiate impacts of surface pollution sources (i.e., altitudinal weightings $\boldsymbol{w_h}$, h = 1~5), including '*within PBL*' ($H < PBLH_{AV}$, assumed altitudinal weighting of 100% from surface pollution source, $\boldsymbol{w_{h1}}$ = 100%), '*below the top of PBL*' ($PBLH_{AV} < H < PBLH_{AV+1\times SD}$, *assumed* $\boldsymbol{w_{h2}}$ = 90%), '*at the top of PBL*' ($PBLH_{AV+1\times SD} < H < PBLH_{AV+2\times SD}$, *assumed* $\boldsymbol{w_{h3}}$ = 70%), '*above PBL*' ($PBLH_{AV+2\times SD} < H < PBLH_{Max}$, *assumed* $\boldsymbol{w_{h4}}$ = 40%) and '*free troposphere*' ($H > PBLH_{Max}$, *assumed* $\boldsymbol{w_{h5}}$ = 0%). Parameter $\boldsymbol{F_{i,j}}$ (in ng m^{-2} day^{-1}) linked to a grid cell ($\boldsymbol{i, j}$) allows to distinguish contributions of air masses in the five altitudinal layers (Eq. 3). This reflects the average potential contribution of incoming air masses in the grid cell ($\boldsymbol{i, j}$) to the receptor site during $\boldsymbol{v}$ sampling campaigns.

$$\boldsymbol{F_{i,j}} = \frac{\sum_{k=1}^{v}[\boldsymbol{F_k}\times\sum_{h=1}^{5}(\boldsymbol{\tau_{i,j,k,h}}\times\boldsymbol{w_h})]}{\sum_{k=1}^{v}[\sum_{h=1}^{5}(\boldsymbol{\tau_{i,j,h}}\times\boldsymbol{w_h})]} \qquad (3)$$

where F_k (in ng m^{-2} day^{-1}) denotes the atmospheric deposition flux of PAHs in the k^{th} sampling campaign, and $\tau_{i,j,k,h}$ is the number of trajectory endpoints (reflecting residence time of an air mass) in the grid cell (i, j) within the altitudinal layer of h belonging to a trajectory corresponding to campaign k.

A weight function related to endpoint number density (w_{ep}, see Eq. 5) was applied to diminish potential extreme or highly uncertain values of $F_{i,j}$ due to marginal numbers of trajectory endpoints in the grid cells far away from receptor site (Eq. 4). Weighted average deposition fluxes ($WADF_{i,j}$) indicate the contribution of surface pollution sources in the grid cell (i, j) to the observed deposition fluxes of PAHs at receptor site:

$$WADF_{i,j} = F_{i,j} \times w_{ep} \quad (4)$$

$$w_{ep} = \begin{cases} 1.00 & (n_{70\%} \le n_{ep}) \\ 0.90 & (n_{80\%} \le n_{ep} < n_{70\%}) \\ 0.50 & (n_{90\%} \le n_{ep} < n_{80\%}) \\ 0.05 & (< n_{90\%}) \end{cases} \quad (5)$$

where $n_{x\%}$ represents the endpoint number in the grid cell, including which the trajectory endpoints accumulated up to x % of the total endpoint number (sorting grid cells from the largest to the lowest according to their endpoint number density as shown in Fig. 4). More details on endpoints are presented in Table S4 of the SI.

Finally, an index of potential source area $I_{PSA}(i.j)$ is calculated by a parameter quotient of $WADF_{i,j}$ to the sampling site cell $WADF_{sampling}$ (Eq. 6) for capturing the 'intensity' of probability that the grid cell ($i.j$) is a potential source area:

$$I_{PSA}(i,j) = \frac{WADF_{i.j}}{WADF_{sampling}} \quad (6)$$

3 RESULTS AND DISCUSSION

3.1 Time series analysis of atmospheric deposition fluxes of PAHs

In our previous work, a three-year-period monitoring of PAH deposition fluxes revealed a possible decreasing trend in urban areas of Shanghai (Feng et al.,

2017). Our new study showed declining deposition fluxes with statistical significance ($p < 0.01$) over eight years at the city center of Shanghai (site SH1) with a half-life time of 1.89 ± 0.53 years at the 95% confidence level (see Figure S1). It is important to point out that the half-life time is not based on a mechanistical model, just a statistical description of the declining fluxes following the approach of Hites (2019). This analysis was conducted at each site and results are listed in Table 1. Except for Chongming Island (SH5) and Yangshan Port (SH6) with a relatively short duration (ca. 3 – 4 years, $p > 0.05$), most of sampling sites covering Shanghai, Jiangsu and Zhejiang revealed ever-decreasing deposition fluxes of atmospheric PAHs over the eight years with statistical significance ($p < 0.01$).

Since atmospheric deposition of PAHs is related closely to air pollutants, such as $PM_{2.5}$, PM_{10}, SO_2 and NO_2, time series of the four pollutants from 2014 to 2020 were also analyzed in Shanghai, Jiaxing and Haimen, respectively. The results are presented in Figures S2 – S4 and Table S3 (SI). The half-life times of PAH deposition fluxes (1.08 – 6.04 yrs at 95% confidence level) were comparable to those of $PM_{2.5}$, PM_{10} and SO_2 (2.83 – 7.58 yrs), while NO_2 showed longer half-life times (11 – 23 yrs) in Shanghai and Jiaxing, and no trend in Haimen ($p = 0.87$). This indicates that decreasing deposition fluxes resulted probably from controlling coal combustion linked to SO_2 emissions rather than petroleum combustion related to NO_2 emissions (Otmani et al., 2020). Dust emission in Shanghai decreased sharply from 141,700 tons in 2014 to 14,800 tons in 2019, while SO_2 emission decreased from 188,100 tons to 7,600 tons in the same time period (Shanghai Statistical Yearbook, 2021). These decreasing trends are thus likely attributed to the Airborne Pollution Prevention and Control Action Plan implemented in 2013 (Zhu et al., 2021), which indirectly reduced atmospheric deposition of PAHs. Although these results indicate an exponential decline of atmospheric pollution and deposition fluxes; they will finally approach a local background level, which is not known so far but likely comparable with the current level in urban areas in southwestern Germany as reported by Liu et al. (2022).

3.2 Contributions of local emission and regional transport

Contributions of regional transport and local emission to PAH deposition fluxes in Shanghai were estimated to explore whether the emission reduction is limited only to local measures or results from measures on large regional scales. Figure 2 depicts spatial variation of PAH deposition fluxes. Sites SH1 (close to the city center) and SH3 (near an industrial area) were strongly influenced by local emissions and subjected to greater deposition fluxes than other sites by a paired-samples *t* test ($p < 0.05$). Fluxes greater than background reflected the contribution of local emission. It is a challenge to select suitable background sites, since theoretically they should be upwind and free from local emissions at any time. However, monsoon climate controls this region and main wind directions change seasonally in Shanghai. No ideal background site existed and only sites with relatively low deposition fluxes could be considered as reference (Pu et al., 2020). The mean value of these sites, including SH4, SH5, SH6, and HM, was used to indicate the background level of this region. Arithmetic (for normal distribution) or geometric mean (for log-normal distribution) values were assumed to reflect the background level in this region or be representative of deposition fluxes at each site. Both of them were used to estimate contribution of local emissions at each site (see equation in Figure 2). Local emissions accounted for 35 – 73% of the total deposition fluxes in Shanghai and 25 – 36% at site JX of Zhejiang. Since the defined background sites could yet be affected by local emissions to a low extent, the contribution of local emissions might be underestimated. Consequently, regional transport is an important contributor to atmospheric deposition of PAHs. Meanwhile, the significant contribution from local emissions could disturb identification of potential source areas for regional transport, if based on time series measurement at one sampling site (further discussion in below).

3.3 Trajectory sector analysis and spatial variation of trajectory endpoint

The influence of air mass origin was investigated by trajectory sector analysis (Dimitriou et al., 2021; Zhu et al., 2011). In Figure 3.a, trajectory endpoints were linked to deposition fluxes of PAHs. Wind directions were divided into sixteen sectors of 22.5°. Average deposition fluxes and percentages of endpoints in each sector were statistically calculated after removing the last 6 hours trajectory

endpoints (close to the receptor site of SH1) to minimize impact from local emissions (Zhu et al., 2011). Elevated deposition fluxes (> 2400 ng m^{-2} day^{-1}) were observed in the sectors of S6-S7 and associated with northwesterly winds, indicating a significant contribution of regional transport from northwestern part of China to Shanghai. Liu et al. (2021) also reported that regional transport from the north-to-northwest of Shanghai was the most plausible contributor of elevated $PM_{2.5}$ and VOCs in winter.

Figure 3.a reveals a large spatial variation in trajectory endpoint density. More endpoints were concentrated at the receptor site(s), for example, endpoint number density n = 3905 in the grid cell containing the receptor site. Specifically, 50% of the total endpoints (n > 80 count per cell (CPC), see Figure 3.b) were located only in the Jiangsu – Zhejiang – Shanghai region (see red cell circle in Figure 3.a), 70% of total (n > 32 CPC) extended to the Shandong and Anhui region, and 80% of total (n > 15 CPC) was further distributed to the Beijing – Tianjin – Hebei region as well as to Henan, Jiangxi, and Fujian, and even the western part of Korea (see yellow circle). The residual 20% of endpoints was scattered widely in a marginal area with a low endpoint number density (n ≤ 15 CPC). The endpoint number density influences uncertainty of estimation in a probabilistic model (Hafner and Hites, 2003), such as CWT and PSCF models. Therefore, the spatial variation of trajectory endpoint was related to the weighting function correction (w_{ep}) further discussed in below.

3.4 Multisite joint location of potential source areas based on an enhanced 3D – CWT model

3.4.1 PBLH and altitudinal weighting (w_h)

Atmospheric pollutants emitted from the ground enter the planetary boundary layer (*PBL*) and undergo regional and long-range transport (Stojic and Stojic, 2017). The height above the ground (*H*) of the air mass is crucial for further geographical transport assessment (Kim et al., 2016). The planetary boundary layer height (*PBLH*), however, is highly dynamic over time and location as shown in Figures S5 – S6 in the SI. PBLH on land followed an exponential distribution in Figure S6.a whereas a log-normal distribution was observed over the sea in Figure S6.b. The standard deviation of PBLH reflects its variability and an

enhanced variability is related to more active convection within boundary layer (Qu et al., 2017). Descriptive statistics of mean (*AV*) as well as standard deviation (*SD*) of *PBLH* reflect the probability that the air mass is within the planetary boundary layer, although there is still a large uncertainty. Here, the height (*H*) of air mass was categorized and given weighting according to likelihood of receiving ground pollution (see details in the Section 2.5). This statistical approach considered the spatial and temporal variations of *PBLH* rather than an arbitrary threshold height of 1000 m in the previous work (Dimitriou et al., 2021).

3.4.2 Weighting function correction (w_{ep}) for the grid cells with a low endpoint number density

In order to reduce uncertainty in the grid cells with a low endpoint number density, an arbitrary or empirical weighting function related to average number of trajectory endpoints in all grid cells ($\boldsymbol{n_{ep,av}}$) was used, as shown in Figure 4.a and Table S4; this allows to correct results of concentration weighted trajectory (CWT) or potential sources contribution function (PSCF) models (Peng et al., 2019; Wei et al., 2019). In this study, trajectories of air masses covered a large geographical domain with a total number of grid cells up to 38,192 and a $\boldsymbol{n_{ep,av}}$ value of 1.28 – 3.65 (see Table S4). In Figure 4.a, the $\boldsymbol{n_{ep,av}}$–based weighting function ($\boldsymbol{w_{ep}}$) did not seem to effectively reduce the uncertainty of average deposition fluxes in the grid cells with a low endpoint number density, so that significant contributions from Nei Mongol and Mongolia were screened, even from the region of Ryukyu Islands where PAH emissions are expected to be very low. Consequently, it is difficult to screen the marginal cells based on average number of trajectory endpoints. An alternative is to shift the highlight from the marginal cells (with lower endpoint number density) to the non-marginal cells (with higher endpoint density). According to the above analysis on spatial variation of trajectory endpoints, an accumulative percentage of 80% was recommended to define the non-marginal and marginal cells (see Figure 3.b) in this study. Hence, we proposed an alternative weighting function $\boldsymbol{w_{ep}}$ (see Figure 3.b) which is connected to the percentage of endpoints in a grid cell to the total. Figure 4.b reveals potential source areas of atmospheric deposition of PAHs more rationally in comparison with Figure 4.a.

3.4.3 Multisite joint location of source area

Spatial origin analysis using CWT or PSCF methods assumes a negligible contribution of local emission or dominance of regional transport to atmospheric pollutants at receptor site (Huang et al., 2021; Suzuki et al., 2021), or requires additional upwind/downwind field sampling to verify modeling results (Hsu et al., 2003). In this study, local emissions were not negligible, probably leading to a false identification of source areas, e.g., high values of weighted average deposition fluxes (***WADF***) in East China Sea (Figure 4). The eight sampling sites were located in a small area and suffered probably from similar regional transport. It is safe to assume the same patterns of regional transport at all sampling sites. A multisite joint location approach was proposed to reduce uncertainties from disturbance of local emissions on locating source areas of regional transport and the limited sample size at the receptor site. In order to improve comparability of CWT results (i.e., ***WADF***) among the sampling sites, the ***WADF*** parameter was transformed into a probabilistic parameter called the index of potential source areas (I_{PSA}) as Eq. 6. Values of $I_{PSA} > 1$ imply that the grid cell is a potential source area for PAH deposition at the receptor site. Slight differences in I_{PSA} maps at eight sampling sites (see Figure S7) are attributed possibly to false identification of potential source areas. Arithmetic and geometric means were used to homogenize the difference, respectively (see Figures 5 and S8); here the geometric mean seemed more rational because I_{PSA} values in marginal cells seem to follow a skewed distribution (not tested statistically due to limited sample size).

As shown in Figure 5, potential source areas of PAH deposition in Shanghai may be grouped in three regions, (a) from Hebei and Tianjin to the middle part of Shandong, over the Yellow Sea, to the eastern part of Jiangsu, (b) from the southwestern part of Shandong to the junction of Anhui and Jiangsu, and (c) from the middle part of Anhui to the northern part of Zhejiang. Similarly, Jiangsu, Anhui and Zhejiang were identified as potential major source areas for atmospheric PAHs and black carbon (Peng et al., 2019; Wei et al., 2019) in Shanghai. With regard to locating the eastern part of the Yellow Sea as potential source areas, a possible explanation is that marine traffic across the Yellow Sea

emitted PAHs through petroleum combustion (Su et al., 2021); alternatively, the Yellow Sea might have been identified by mistake due to the limited sample size and the fact that the Yellow Sea happens to be located in the major pathway of air masses moving to Shanghai. It is worth noting that each grid cell with high I_{PSA} value does not necessarily indicate a source area, but a group of cells together has more credence (Hafner and Hites, 2003; Sheng et al., 2013).

The locations of potential source areas were further cross-validated by ground observation of atmospheric pollutants. Annual mean concentrations of $PM_{2.5}$, PM_{10}, SO_2 and NO_2 in the years of 2014 and 2018 were calculated respectively at 1,493 national ground observation stations over the mainland of China, and their spatial distributions, as well as the $\boldsymbol{I_{PSA}}$ map of PAH deposition, are illustrated in Figure S9 – S12. Higher concentrations of PM_x and SO_2 were observed in the source areas identified above, for example, Hebei, Tianjin, Shandong and Anhui, where the concentrations of PM_x and SO_2, excluding NO_2, decreased significantly during 2014 – 2018. This further demonstrates the remarkable achievement of emission reduction in coal combustion rather than petroleum combustion on a national scale of China.

4. CONCLUSIONS

An enhanced 3D – CWT model was developed with a comprehensive consideration of spatial and temporal variations of the planetary boundary layer height. A probabilistic parameter called the index of potential source area ($\boldsymbol{I_{PSA}}$) was proposed to quantify and normalize the probability that grid cells are source areas in order to achieve multisite joint location based on the 3D – CWT model. Geometric mean values of $\boldsymbol{I_{PSA}}$ were recommended to homogenize the locating results at eight sampling sites.

Declining deposition fluxes of atmospheric PAHs were observed with statistical significance in Shanghai and its surrounding areas. Regional transport was an important contributor of PAH deposition in Shanghai and attributed to the northwestern parts of China. The multisite joint location method successfully identified potential source areas, including Hebei, Tianjin, Shandong and Jiangsu to the north of Shanghai, and Anhui to the west of Shanghai. The spatial distribution of primary air pollutants and their concentration change between

the two years of 2014 and 2018 further confirmed their spatial origin. The declining atmospheric deposition of PAHs is likely attributed to emission reduction on local scale (Shanghai) and on a national scale of China. This study thus provides evidence to support the effectiveness of the Airborne Pollution Prevention and Control Action Plan in China implemented since 2013.

ASSOCIATED CONTENT

SUPPORTING INFORMATION

Detailed information on sampling, chemical analysis, QA/QC, time series analysis, backward trajectory analysis and data source of air quality observation datasets of China can be found.

DECLARATION OF COMPETING INTEREST

The authors declare that they have no known competing financial interests or personal relationships that could have appeared to influence the work reported in this paper.

AUTHORS CONTRIBUTION

Ying Liu: Conceptualization; Investigation; Visualization; ; Supervision; Writing – original draft, reviewing & editing.

Xiaomin Zhang: Investigation – HYSPLIT;

Jianguo Tan: Conceptualization; Writing – Reviewing & editing;

Peter Grathwohl: Conceptualization; Writing – Reviewing & editing;

Rainer Lohmann: Writing – Reviewing & editing;

ACKNOWLEDGEMENTS

We acknowledge funding from the National Natural Science Foundation of China (Nos.: 21876126 and 22176144). We would like to thank Yi Gao, Lirong Zheng, Shuya Xie, Tongtong Li and Junyi Yu from Tongji University for sampling and chemical analysis. We also thank Admir Créso Targino and two anonymous reviewers for helpful comments and suggestions.

REFERENCES

Arellano, L., Fernández, P., van Drooge, B.L., Rose, N.L., Nickus, U., Thies, H., Stuchlík, E., Camarero, L., Catalan, J., Grimalt, J.O., 2018. Drivers of atmospheric deposition of polycyclic aromatic hydrocarbons at European high-altitude sites. Atmospheric Chemistry and Physics 18, 16081-16097.

Bao, Z., Chen, L., Li, K., Han, L., Wu, X., Gao, X., Azzi, M., Cen, K., 2019. Meteorological and chemical impacts on PM2.5 during a haze episode in a heavily polluted basin city of eastern China. Environmental Pollution 250, 520-529.

Shanghai Municipal Statistics Bureau, 2021. Shanghai Statistical Yearbook 2020. China Statistics Press.

Charlson, R.J., 2000. 7 - The Atmosphere, in: Jacobson, M.C., Charlson, R.J., Rodhe, H., Orians, G.H. (Eds.), International Geophysics. Academic Press, pp. 132-158.

Cheng, C., Bi, C.J., Wang, D.Q., Yu, Z.J., Chen, Z.L., 2018. Atmospheric deposition of polycyclic aromatic hydrocarbons (PAHs) in Shanghai: the spatio-temporal variation and source identification. Frontiers of Earth Science 12, 63-71.

Dee, D.P., Uppala, S.M., Simmons, A.J., Berrisford, P., Poli, P., Kobayashi, S., Andrae, U., Balmaseda, M.A., Balsamo, G., Bauer, P., Bechtold, P., Beljaars, A.C.M., van de Berg, L., Bidlot, J., Bormann, N., Delsol, C., Dragani, R., Fuentes, M., Geer, A.J., Haimberger, L., Healy, S.B., Hersbach, H., Holm, E.V., Isaksen, L., Kallberg, P., Kohler, M., Matricardi, M., McNally, A.P., Monge-Sanz, B.M., Morcrette, J.J., Park, B.K., Peubey, C., de Rosnay, P., Tavolato, C., Thepaut, J.N., Vitart, F., 2011. The ERA-Interim reanalysis: configuration and performance of the data assimilation system. Quarterly Journal of the Royal Meteorological Society 137, 553-597.

Degrendele, C., Audy, O., Hofman, J., Kucerik, J., Kukucka, P., Mulder, M.D., Pribylova, P., Prokes, R., Sanka, M., Schaumann, G.E., Lammel, G., 2016. Diurnal Variations of Air-Soil Exchange of Semivolatile Organic Compounds (PAHs, PCBs, OCPs, and PBDEs) in a Central European Receptor Area. Environmental Science & Technology 50, 4278-4288.

Dimitriou, K., Mihalopoulos, N., Leeson, S.R., Twigg, M.M., 2021. Sources of PM2.5-bound water soluble ions at EMEP's Auchencorth Moss (UK) supersite revealed by 3D-Concentration Weighted Trajectory (CWT) model. Chemosphere 274, 129979.

Dimitriou, K., Tsagkaraki, M., Zarmpas, P., Mihalopoulos, N., 2022. Impact of spatial and vertical distribution of air masses on PM10 chemical components at the Eastern Mediterranean – A seasonal approach. Atmospheric Research 266.

Dumanoglu, Y., Gaga, E.O., Gungormus, E., Sofuoglu, S.C., Odabasi, M., 2017. Spatial and seasonal variations, sources, air-soil exchange, and carcinogenic risk assessment for PAHs and PCBs in air and soil of Kutahya, Turkey, the province of thermal power plants. Science of the Total Environment 580, 920-935.

Feng, D.L., Liu, Y., Gao, Y., Zhou, J.X., Zheng, L.R., Qiao, G., Ma, L.M., Lin, Z.F., Grathwohl, P., 2017. Atmospheric bulk deposition of polycyclic aromatic hydrocarbons in Shanghai: Temporal and spatial variation, and global comparison. Environmental Pollution 230, 639-647.

Hafner, W.D., Hites, R.A., 2003. Potential sources of pesticides, PCBs, and PAHs to the atmosphere of the Great Lakes. Environmental Science & Technology 37, 3764-3773.

Hites, R.A., 2019. Statistical Approach for Assessing the Stockholm Convention's Effectiveness: Great Lakes Atmospheric Data. Environmental Science & Technology 53, 8585-8590.

Hites, R.A., 2021. Polycyclic Aromatic Hydrocarbons in the Atmosphere near the Great Lakes: Why

Do Their Concentrations Vary? Environmental Science & Technology 55, 9444-9449.
Hosseini Dehshiri, S.S., Firoozabadi, B., Afshin, H., 2022. A new application of multi-criteria decision making in identifying critical dust sources and comparing three common receptor-based models. Science of the Total Environment 808, 152109.
Hsu, Y.K., Holsen, T.M., Hopke, P.K., 2003. Comparison of hybrid receptor models to locate PCB sources in Chicago. Atmospheric Environment 37, 545-562.
Hu, T.P., Mao, Y., Ke, Y.P., Liu, W.J., Cheng, C., Shi, M.M., Zhang, Z.Q., Zhang, J.Q., Qi, S.H., Xing, X.L., 2021. Spatial and seasonal variations of PAHs in soil, air, and atmospheric bulk deposition along the plain to mountain transect in Hubei province, central China: Air-soil exchange and long-range atmospheric transport. Environmental Pollution 291, 118139.
Huang, H.Y., Liu, B.S., Li, S., Choe, T.H., Dai, Q.L., Gu, Y., Diao, L.L., Zhang, S.F., Bi, X.H., Luo, Z.W., Lu, M.M., Zhang, Y.F., Feng, Y.C., 2021. An estimation method for regional transport contributions from emission sources based on a high-mountain site: a case study in Zhumadian, China. Atmospheric Environment 263.
Jia, J.P., Bi, C.J., Zhang, J.F., Chen, Z.L., 2019. Atmospheric deposition and vegetable uptake of polycyclic aromatic hydrocarbons (PAHs) based on experimental and computational simulations. Atmospheric Environment 204, 135-141.
Keyte, I.J., Harrison, R.M., Lammel, G., 2013. Chemical reactivity and long-range transport potential of polycyclic aromatic hydrocarbons - a review. Chemical Society Reviews 42, 9333-9391.
Kim, I.S., Wee, D., Kim, Y.P., Lee, J.Y., 2016. Development and application of three-dimensional potential source contribution function (3D-PSCF). Environmental Science and Pollution Research 23, 16946-16954.
Lammel, G., 2015. Polycyclic Aromatic Compounds in the Atmosphere - A Review Identifying Research Needs. Polycyclic Aromatic Compounds 35, 316-329.
Li, J., Han, Y., Liu, W., Wang, S., Cao, L., Lu, Z., 2021a. A new theoretical model deriving planetary boundary layer height in desert regions and its application on dust devil emissions. Science of the Total Environment 814, 152378.
Li, X.B., Fan, G.Q., Lou, S.R., Yuan, B., Wang, X.M., Shao, M., 2021b. Transport and boundary layer interaction contribution to extremely high surface ozone levels in eastern China. Environmental Pollution 268.
Lian, J.J., Ren, Y., Chen, J.M., Wang, T., Cheng, T.T., 2009. Distribution and source of alkyl polycyclic aromatic hydrocarbons in dustfall in Shanghai, China: the effect on the coastal area. J Environ Monit 11, 187-192.
Liang, J., Fang, H., Wu, L., Zhang, T., Wang, X., 2016. Characterization, Distribution, and Source Analysis of Metals and Polycyclic Aromatic Hydrocarbons (PAHs) of Atmospheric Bulk Deposition in Shanghai, China. Water, Air, & Soil Pollution 227.
Liu, C., Fu, X., Zhang, H., Ming, L., Xu, H., Zhang, L., Feng, X., 2019. Sources and outflows of atmospheric mercury at Mt. Changbai, northeastern China. Science of the Total Environment 663, 275-284.
Liu, J., Jia, J., Grathwohl, P., 2022. Dilution of concentrations of PAHs from atmospheric particles, bulk deposition to soil: a review. Environ Geochem Health.
Liu, Y., Gao, Y., Yu, N., Zhang, C., Wang, S., Ma, L., Zhao, J., Lohmann, R., 2015. Particulate matter, gaseous and particulate polycyclic aromatic hydrocarbons (PAHs) in an urban traffic tunnel of

China: Emission from on-road vehicles and gas-particle partitioning. Chemosphere 134, 52-59.
Liu, Y., Wang, H., Jing, S., Peng, Y., Gao, Y., Yan, R., Wang, Q., Lou, S., Cheng, T., Huang, C., 2021. Strong regional transport of volatile organic compounds (VOCs) during wintertime in Shanghai megacity of China. Atmospheric Environment 244.
Masiol, M., Squizzato, S., Rich, D.Q., Hopke, P.K., 2019. Long-term trends (2005-2016) of source apportioned PM2.5 across New York State. Atmospheric Environment 201, 110-120.
Miao, Y.C., Che, H.Z., Zhang, X.Y., Liu, S.H., 2021. Relationship between summertime concurring PM2.5 and O-3 pollution and boundary layer height differs between Beijing and Shanghai, China. Environmental Pollution 268.
Otmani, A., Benchrif, A., Tahri, M., Bounakhla, M., Chakir, E.M., El Bouch, M., Krombi, M., 2020. Impact of Covid-19 lockdown on PM10, SO2 and NO2 concentrations in Sale City (Morocco). Science of the Total Environment 735, 139541.
Peng, J., Grimmond, C.S.B., Fu, X.S., Chang, Y.Y., Zhang, G.L., Guo, J.B., Tang, C.Y., Gao, J., Xu, X.D., Tan, J.G., 2017. Ceilometer-Based Analysis of Shanghai's Boundary Layer Height (under Rain- and Fog-Free Conditions). Journal of Atmospheric and Oceanic Technology 34, 749-764.
Peng, X., Liu, M., Zhang, Y., Meng, Z., Achal, V., Zhou, T., Long, L., She, Q., 2019. The characteristics and local-regional contributions of atmospheric black carbon over urban and suburban locations in Shanghai, China. Environmental Pollution 255.
Polissar, A.V., Hopke, P.K., Harris, J.M., 2001. Source regions for atmospheric aerosol measured at Barrow, Alaska. Environmental Science & Technology 35, 4214-4226.
Pu, W.W., Ma, Z.Q., Collett, J.L., Guo, H., Lin, W.L., Cheng, Y., Quan, W.J., Li, Y.R., Dong, F., He, D., 2020. Regional transport and urban emissions are important ammonia contributors in Beijing, China. Environmental Pollution 265.
Qu, Y.W., Han, Y., Wu, Y.H., Gao, P., Wang, T.J., 2017. Study of PBLH and Its Correlation with Particulate Matter from One-Year Observation over Nanjing, Southeast China. Remote Sensing 9.
Sheng, J.J., Wang, X.P., Gong, P., Joswiak, D.R., Tian, L.D., Yao, T.D., Jones, K.C., 2013. Monsoon-Driven Transport of Organochlorine Pesticides and Polychlorinated Biphenyls to the Tibetan Plateau: Three Year Atmospheric Monitoring Study. Environmental Science & Technology 47, 3199-3208.
Stein, A.F., Draxler, R.R., Rolph, G.D., Stunder, B.J.B., Cohen, M.D., Ngan, F., 2015. Noaa's Hysplit Atmospheric Transport and Dispersion Modeling System. Bulletin of the American Meteorological Society 96, 2059-2077.
Stojic, A., Stojic, S.S., 2017. The innovative concept of three-dimensional hybrid receptor modeling. Atmospheric Environment 164, 216-223.
Su, P.H., Yue, H.L., Zhang, W.W., Tomy, G.T., Yin, F., Sun, D., Ding, Y.S., Li, Y.F., Feng, D.L., 2021. Application of a fugacity model to estimate emissions and environmental fate of ship stack PAHs in Shanghai, China. Chemosphere 281.
Sun, J.J., Huang, L., Liao, H., Li, J.Y., Hu, J.L., 2017. Impacts of Regional Transport on Particulate Matter Pollution in China: a Review of Methods and Results. Current Pollution Reports 3, 182-191.
Suzuki, Y., Matsunaga, K., Yamashita, Y., 2021. Assignment of PM2.5 sources in western Japan by non-negative matrix factorization of concentration-weighted trajectories of GED-ICP-MS/MS element concentrations. Environmental Pollution 270.

603 Wang, Q., Liu, M., Li, Y., Liu, Y.K., Li, S.W., Ge, R.R., 2016. Dry and wet deposition of polycyclic
604 aromatic hydrocarbons and comparison with typical media in urban system of Shanghai,
605 China. Atmospheric Environment 144, 175-181.
606 Wang, Y.Q., Zhang, X.Y., Draxler, R.R., 2009. TrajStat: GIS-based software that uses various
607 trajectory statistical analysis methods to identify potential sources from long-term air
608 pollution measurement data. Environmental Modelling & Software 24, 938-939.
609 Wei, X.-Y., Liu, M., Yang, J., Du, W.-N., Sun, X., Huang, Y.-P., Zhang, X., Khalil, S.K., Luo, D.-M., Zhou, Y.-
610 D., 2019. Characterization of PM2.5-bound PAHs and carbonaceous aerosols during three-
611 month severe haze episode in Shanghai, China: Chemical composition, source apportionment
612 and long-range transportation. Atmospheric Environment 203, 1-9.
613 Yan, L., Li, X., Chen, J., Wang, X., Du, J., Ma, L., 2012. Source and deposition of polycyclic aromatic
614 hydrocarbons to Shanghai, China. Journal of Environmental Sciences 24, 116-123.
615 Zhang, K., Shang, X., Herrmann, H., Meng, F., Mo, Z., Chen, J., Lv, W., 2019. Approaches for
616 identifying PM2.5 source types and source areas at a remote background site of South China in
617 spring. Science of the Total Environment 691, 1320-1327.
618 Zhao, N., Wang, G., Li, G., Lang, J., Zhang, H., 2020. Air pollution episodes during the COVID-19
619 outbreak in the Beijing-Tianjin-Hebei region of China: An insight into the transport pathways
620 and source distribution. Environmental Pollution 267.
621 Zhu, F.-J., Ma, W.-L., Hu, P.-T., Zhang, Z.-F., Li, Y.-F., 2021. Temporal trends of atmospheric PAHs:
622 Implications for the influence of the clean air action. Journal of Cleaner Production 296.
623 Zhu, L., Huang, X., Shi, H., Cai, X., Song, Y., 2011. Transport pathways and potential sources of
624 PM10 in Beijing. Atmospheric Environment 45, 594-604.
625
626

627 **Legend of Tables**

628 **Table 1.** Slopes (year^{-1}) and half-life times ($T_{0.5}$ in years) of atmospheric
629 deposition fluxes of 15 PAHs in Shanghai (SH), Haimen (HM) and
630 Jiaxing (JX).

631

632 **Legend of Figures**

633 **Figure1**. Sampling sites of atmospheric bulk deposition of PAHs in Shanghai and
634 its surrounding areas.

635

636 **Figure 2.** Spatial variation and local emission contribution to PAH deposition
637 fluxes at the eight monitoring sites. The horizontal lines represent 1st,
638 50th, and 99th percentiles, and the boxes represent 25th and 75th
639 percentiles.

640

641 **Figure 3.** Arithmetic mean of deposition fluxes of PAHs in sixteen wind direction
642 sectors, their spatial variation (a) and accumulative percentage (b) of
643 endpoint number in backward trajectories to the center of Shanghai
644 (site SH1).

645

646 **Figure 4.** Concentration weighted trajectory (CWT) maps at the receptor site of
647 SH1 (Shanghai) via weighting function (w_{ep}) correction based on
648 average density (a) and accumulative contribution (b) of trajectory
649 endpoint number.

650

651 **Figure 5.** Index of potential source area (I_{PSA}) map of PAH deposition via a
652 geometric mean approach of eight-site joint locating.

Table 1. Slopes (year^{-1}) and half-life times ($T_{0.5}$ in years) of atmospheric deposition fluxes of 15 PAHs in Shanghai (SH), Haimen (HM) and Jiaxing (JX).

Label	Site	Period	Slope	SD_{Slope}	*p*	$T_{0.5}$ (years) [a]
SH1	TJXC	2012-2019	-0.367	0.051	<0.001	1.89 (1.36-2.41)
SH2	JD	2012-2017	-0.249	0.076	0.005	2.78 (1.08-4.47)
SH3	QP	2012-2019	-0.305	0.083	0.002	2.27 (1.02-3.51)
SH4	CXD	2012-2019	-0.180	0.051	0.002	3.86 (1.67-6.04)
SH5	CMD	2012-2014	-0.121	0.201	0.562	No trend
SH6	YSG	2016-2019	0.139	0.163	0.422	No trend
HM	HM	2012-2019	-0.296	0.048	<0.001	2.34 (1.57-3.10)
JX	JX	2012-2019	-0.333	0.047	<0.001	2.08 (1.50-2.66)

[a.] Best estimate with a 95% confidence interval in brackets.

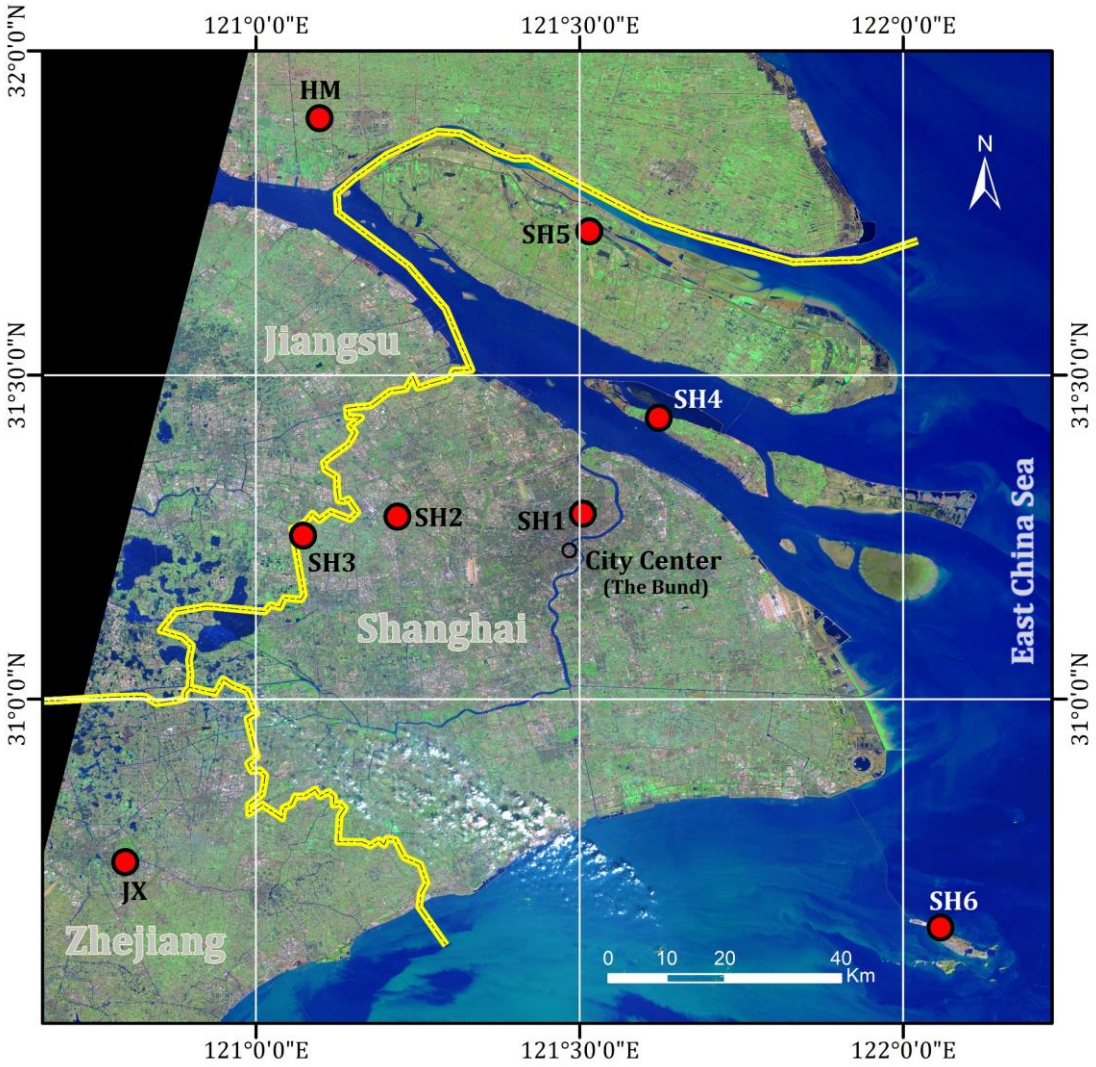

Figure 1. Sampling sites of atmospheric bulk deposition of PAHs in Shanghai and its surrounding areas.

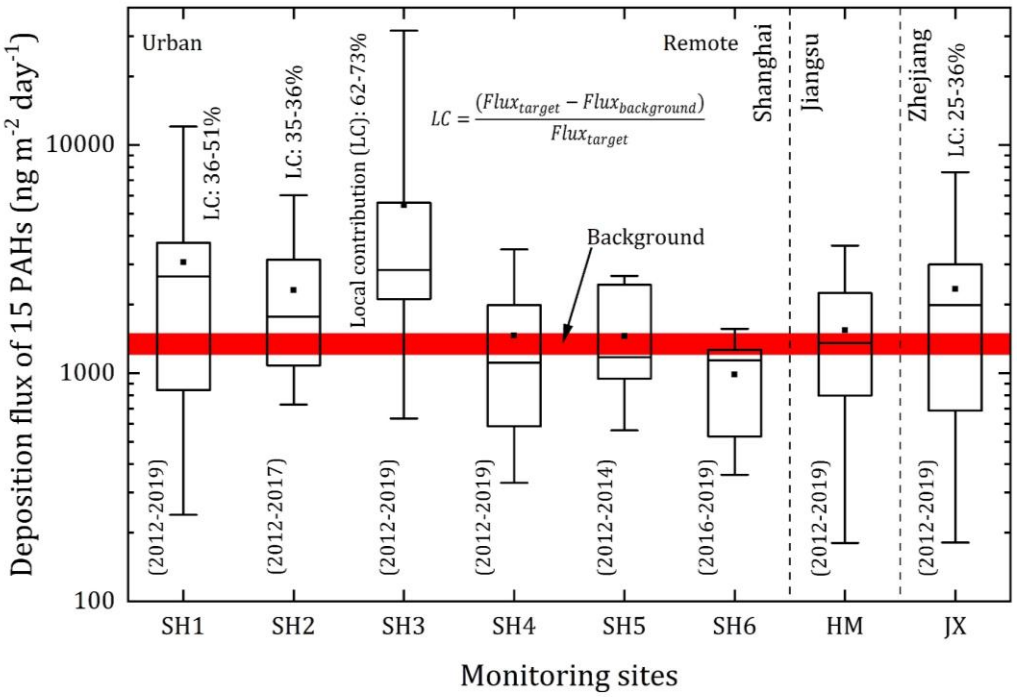

Figure 2. Spatial variation and local emission contribution to PAH deposition fluxes at the eight monitoring sites. The horizontal lines represent 1st, 50th, and 99th percentiles, and the boxes represent 25th and 75th percentiles.

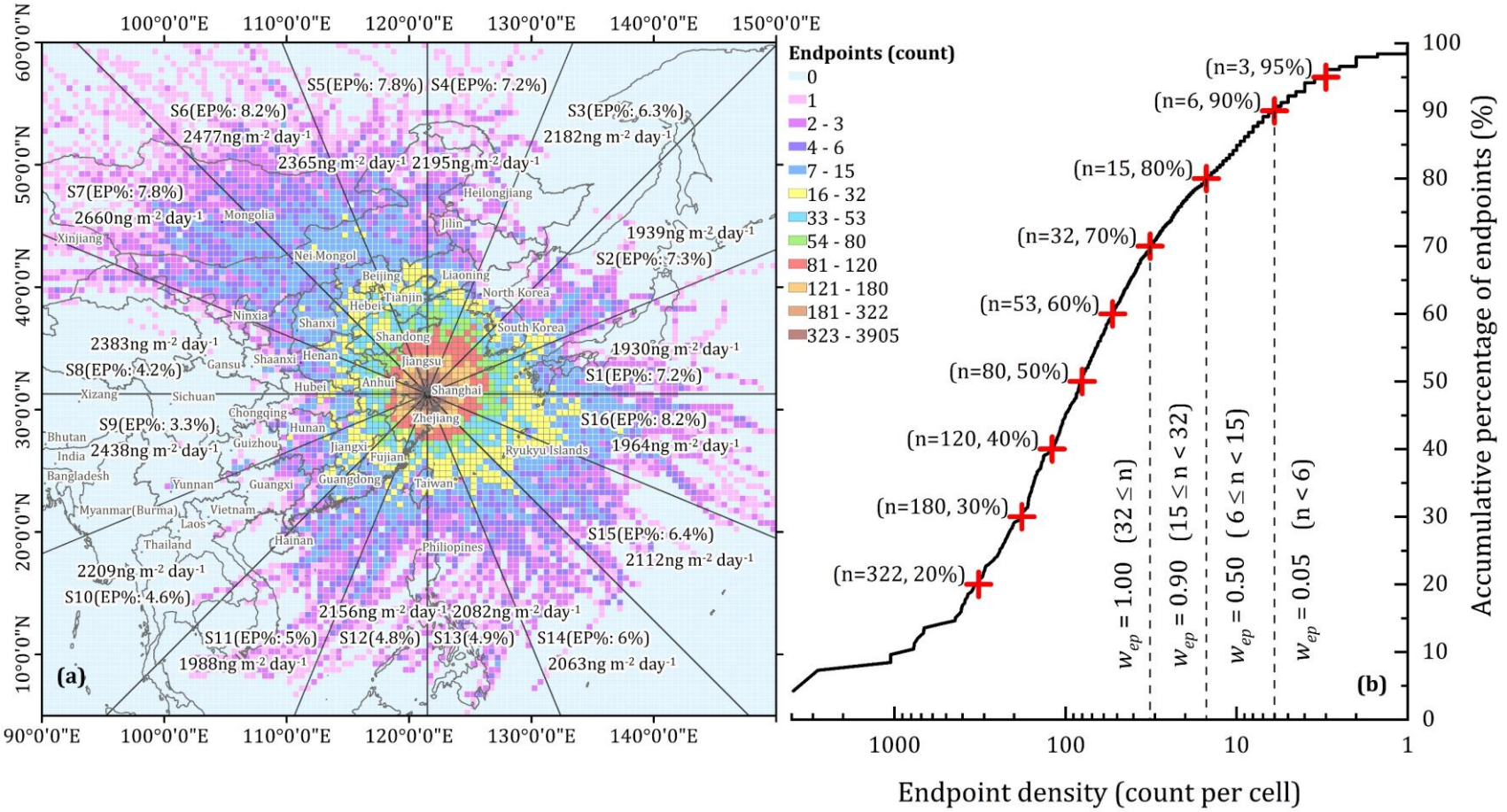

Figure 3. Arithmetic mean of deposition fluxes of PAHs in sixteen wind direction sectors, their spatial variation (a) and accumulative percentage (b) of endpoint number in backward trajectories to the center of Shanghai (site SH1).

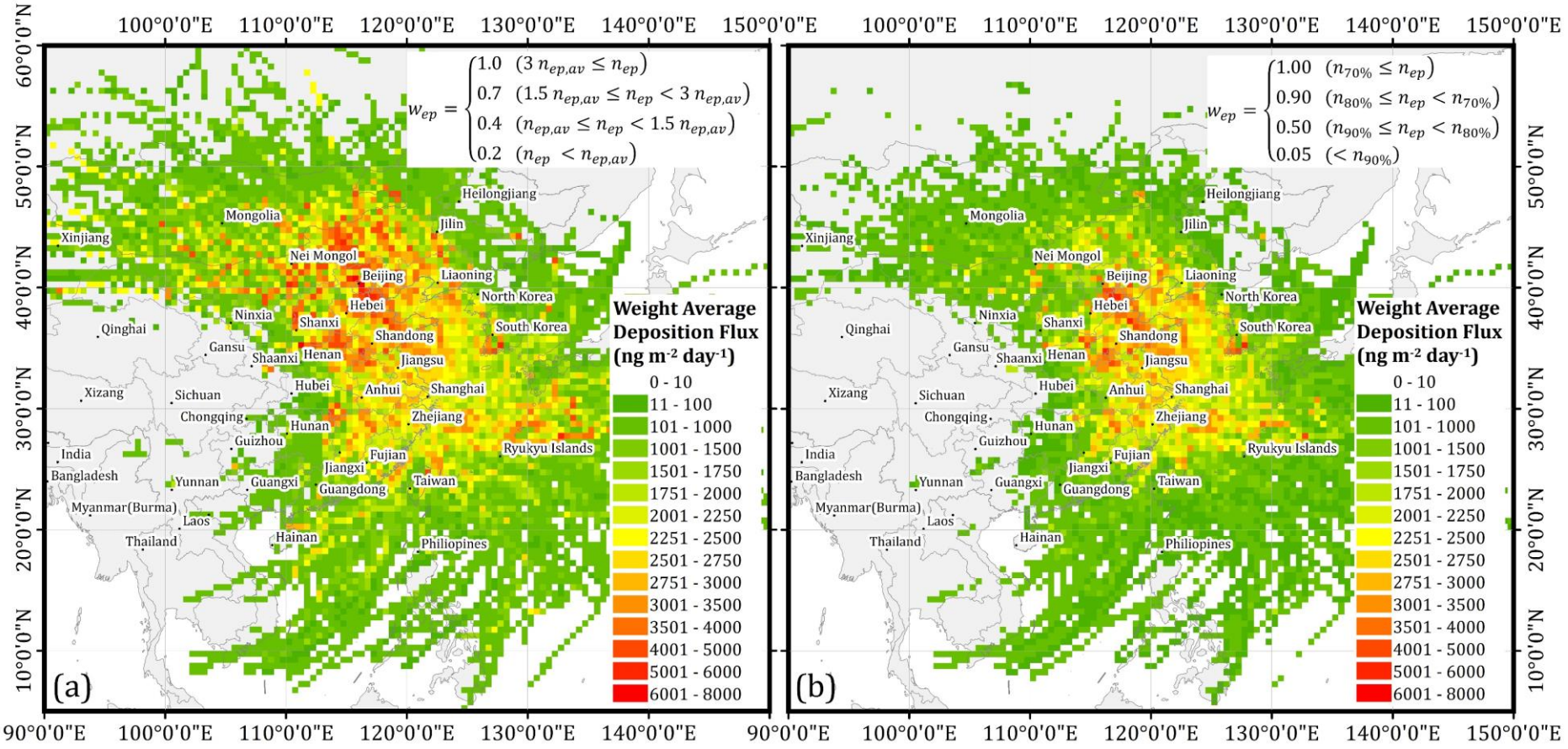

Figure 4. Concentration weighted trajectory (CWT) maps at the receptor site of SH1 (Shanghai) via weighting function (w_{ep}) correction based on average density (a) and accumulative contribution (b) of trajectory endpoint number.

675

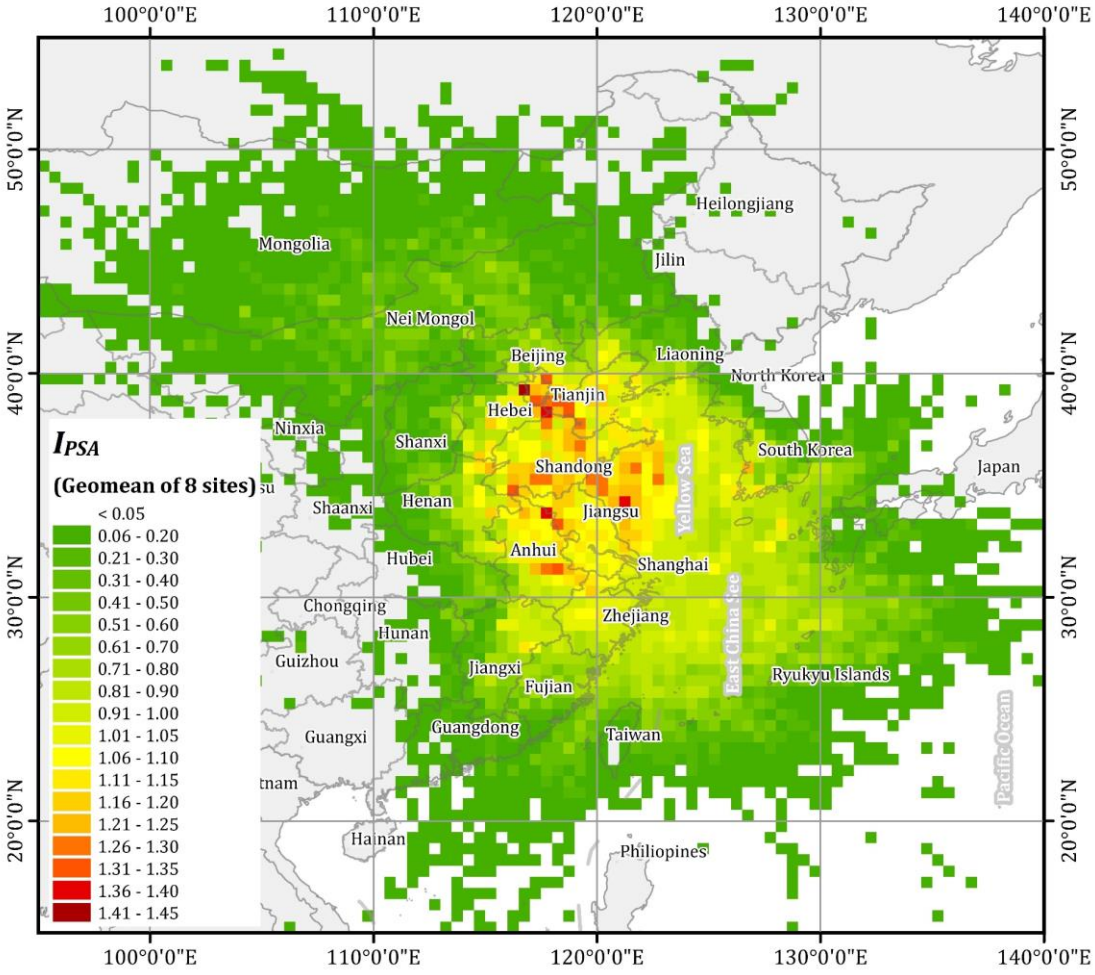

676

677 **Figure 5.** Index of potential source area (I_{PSA}) map of PAH deposition via a geometric mean
678 approach of eight-site joint locating.